5.4 Electronic Structure of Condensed Matter

5-4-1 Polarization Dependence of Soft-X-Ray Raman Scattering: New Experimental Method to Determine the Symmetry of Electronic Structures

Soft X-ray Raman scattering (SXRS) experiments give important information on the interaction of matter and light [1]. SXRS is known to be a bulk-sensitive and site-selective method for probing the electronic states compared to photoelectron spectroscopy. Further, the polarization dependence of SXRS will give new information about the symmetry of the electronic states in the ground state, because SXRS is a second-order optical process described by the Kramers-Heisenberg formula.

We have studied the condition for which the polarization dependence of SXRS could be observed. Fig. 1 shows polarization-dependent SXRS spectra taken using soft X-rays with linear polarization [2, 3]. SXRS is recorded in 'depolarized' and 'polarized' configurations. When SXRS is taken in the depolarized configuration, the polarization vector of the emitted photon rotates by 90° from that of the incident photon. If SXRS is measured in the polarized configuration, the emitted photon contains the same polarization vector as that of the incident photon. Figure 1 shows a clear polarization dependence of the Raman scattering of TiO_2 (rutile) [4].

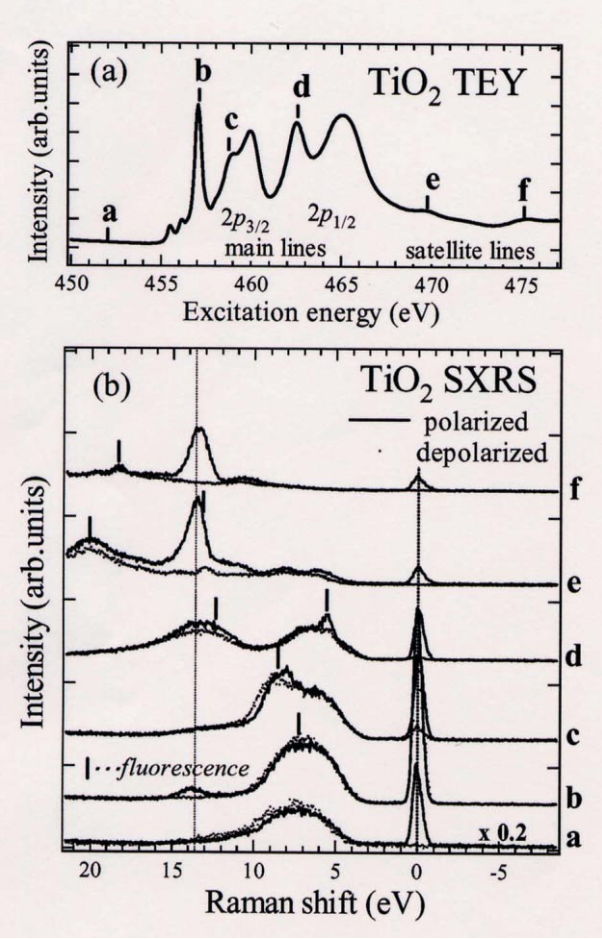

Figure 1
Polarization dependence of the soft X-ray Raman scattering of TiO_2.

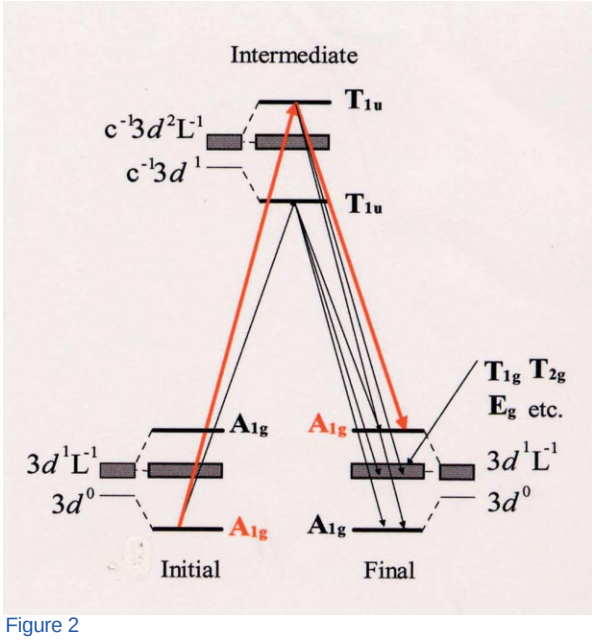

Figure 2
Schematic energy-level diagram and soft X-ray Raman scattering process (arrows) in TiO_2. $c^{-1}$and L^{-1} represent a core hole and a ligand hole.

A strong polarization dependence was observed at a 14-eV Raman shift, as shown by the red curve.

Figure 2 shows a schematic diagram of the electronic states of TiO_2 based on a localized electron picture. The initial and final states are the bonding and antibonding states between the $3d^0$ and $3d^1L^{-1}$ configurations, where $3d^1L^{-1}$ represents a Ti 3*d* electron and a ligand hole. The polarization dependence of the SXRS spectra can be well explained by using Kramers-Heisenberg formula (the arrows in Fig. 2). We find that the existence of the A_{1g} mode in solids is important for the polarization dependence in SXRS. The band calculations do not yield the large 14-eV Raman band energy, whereas the localized electron model can do. Despite no 3*d* electron in TiO_2 (rutile), the electron- correlation effect plays an essential role in the electronic states. The polarization dependence of SXRS is very useful for clarifying the electronic structure of materials.

5-4-2 Evidence for the Existence of a Nitrogen-Substituted Graphite Structure by the Polarization Dependence of NEXAFS

Carbon nitride (CN_x) has attracted much attention because of its characteristic properties such as extreme hardness and many crystal phases [5]. Graphite-like CN_x is interesting due to its promising semiconducting property. However, despite considerable efforts to synthesize CN_x, only a few studies have been reported concerning graphite-like CN_x, because most of the synthesized CN_x films are amorphous, having variety of possible local structures, and long-range order is lacking. To clarify the local structures, we measured the NEXAFS spectra of CN_x films.

CN_x thin films were synthesized in situ by nitrogen-ion implantation in highly oriented pyrolitic graphite (HOPG). Ion implantation was performed at room temperature and at 3.0 keV energy. The ion fluence was

1.7×10^{15} ions/cm^2. After the procedure, thin films were annealed for 3 min. The polarization dependence of NEXAFS spectra was studied for samples with different annealing temperatures (T= 840 and 1100°C).

Figure 3 shows the N 1s NEXAFS spectra of CN_x film. The solid and broken curves show the results at grazing (θ = 10°) and normal (θ = 90°) incidence, respectively. Three discrete π* resonances (a, b, and c) were observed. For peaks a and c, the π* resonances are enhanced at grazing incidence and suppressed at normal incidence. This polarization dependence is similar to that of the π* resonance in the C 1s NEXAFS spectra of HOPG. A close inspection shows that the intensity of peak c is enhanced as the annealing temperature increases. In contrast, peak b shows a polarization dependence opposite to that of the other peaks. These results indicate that all of the peaks originate from different local structures.

Three local structures at the nitrogen site are candidates for the origin of the π* resonances. Namely, for the cases of one, two, and three carbon coordination, we can image a cyanic structure, a pyridine-like structure, and a graphite-like structure, respectively. Among them, the pyridine-like and graphite-like structures can have a graphitic orientation. Since the cyanic group is bonded with the graphite plane by a single C-C bond, this structure is expected to have an orientation which is nearly upright to the graphite plane. Peak c is especially enhanced by annealing. We attribute this to a structural change of the graphite crystal. If a graphite crystal damaged by ion implantation is recovered by annealing, pyridine-like structures should change to graphite-like structures. This implies that the graphite-like structures should increase by annealing. Concluding, we ascribe

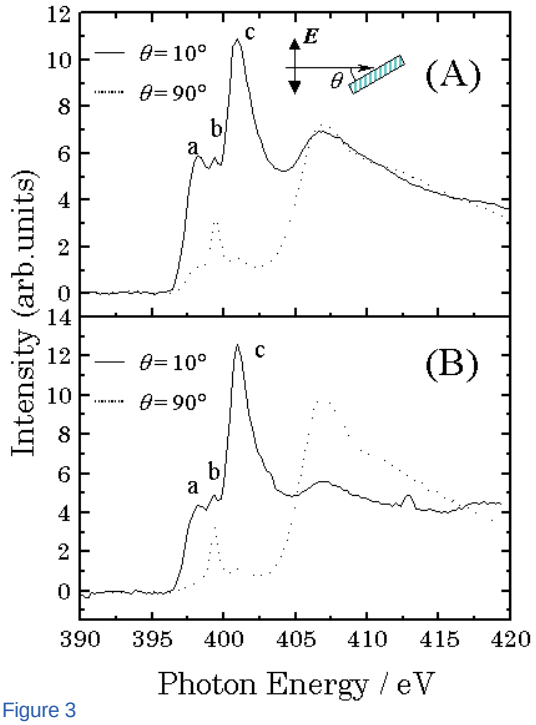

Figure 3
N 1s NEXAFS spectra of CN_x films annealed at (A) 840°C and (B) 1100°C. The solid and dotted lines indicate the spectra for grazing (θ= 10°) and normal (θ= 90°) incidence, respectively.

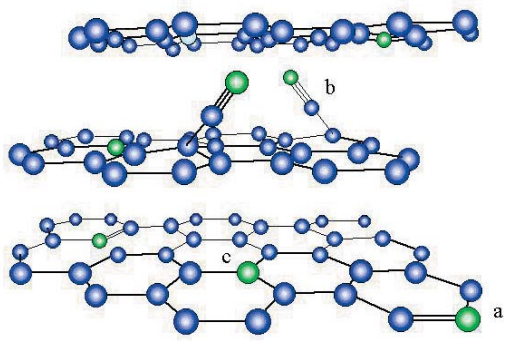

Figure 4.
Schematic diagrams of CN_x local structures in a graphite matrix. The blue balls and green balls show C and N atoms, respectively. a) pyridine- like structure; b) cyanic structure; c) graphite-like structure.

peaks a, b, and c to pyridine-like, cyanic, and graphite-like structure, respectively, as in Fig. 4 [6].

5-4-3 Study of Partial Electronic Density of States of B-2p in MgB_2 Using X-ray Fluorescence Measurement

The discovery of superconducting MgB_2 with a transition temperature of 39 K [7] has stimulated a large number of studies. An efficient step towards understanding the mechanism of superconductivity in MgB_2 is to clarify the difference between this material and non-superconductors such as AlB_2.

First-principle band calculations reveal that a large difference between MgB_2 and AlB_2 is that the σ band plays an important role in superconductivity in MgB_2 [8]. To clarify this issue, we directly observed the partial density of states (PDOS) of B-2*p*σ and 2*p*π bands in MgB_2 and AlB_2 by performing polarization-dependent X-ray emission spectroscopy (XES) and X-ray absorption spectroscopy (XAS) measurements on single crystalline MgB_2 and AlB_2 [9]. By measuring the dipole transition between *2p* and 1*s* core levels of boron, we can specifically probe the PDOS of B 2*p* states. Then, by measuring the polarization dependence of XES and XAS for single crystalline specimens using linear polarization, we could successfully derive the PDOS of B-2*p* σ and 2*p*π bands in MgB_2 and AlB_2 [9].

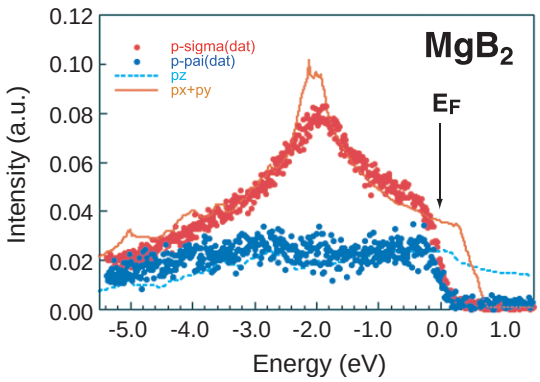

Figure 5
Partial density of states (PDOS) of B-2*p*σ(●) and 2*p*π(●) in MgB_2, derived from fluorescence spectroscopy. Solid and broken lines represent the theoretical PDOS of B-2*p*σ and 2*p*π given by Oguchi, respectively.

Figure 5 shows the PDOS of B-2$p\sigma$ and 2$p\pi$ in MgB_2 derived from fluorescence data. The theoretical PDOS of B-2$p\sigma$ and 2$p\pi$ are shown by the solid (σ) and the broken (π) lines, respectively [8]. We observed significant amounts of PDOS at the Fermi energy in both B-2$p\sigma$ and 2$p\pi$ states for MgB_2. However, for AlB_2, there was almost no PDOS at the Fermi energy in B-2$p\sigma$ and a considerable amount of PDOS at the Fermi energy in B-2$p\pi$, as reported in ref. [9]. The importance of the B-2$p\sigma$ state for superconductivity in MgB_2 was confi rmed

5-4-4 Extraction of a Replicative Multi-Electron Contribution to XANES Spectra by Comparative Soft X-Ray Absorption and Emission Spectroscopy

A detailed study of multielectron excitation processes, *e.g.* shake-up single ionization and shake-off double ionization accompanying inner-shell photoionization, in the near threshold region has recently become possible to investigate intra-atomic electron-electron correlations [10]. The intensities of X-ray satellite or hypersatellite lines arising from core-to-core transitions are measured as a function of the exciting photon energy by X-ray emission spectroscopy (XES). In this study, we have applied this technique to an F-K fluorescence XANES which involves the valence-to-core transitions, and succeeded in determining quantitatively the contribution of multielectron excitation processes to the XANES spectrum [11].

The sample was NaF. The fluorine Kα spectrum was measured using a soft X-ray emission (SXE) spectrometer and the F-K absorption spectrum (XAS) was measured by the total photon yield (TPY) method using a photodiode. Fig. 6 shows the spectral variation of the F Kα emission for NaF as a function of excitation energy. In addition to the $K\alpha_{1,2}$ diagram lines, $K\alpha_{3,4}$ satellite lines were observed near the onset of [1s2p] double excitation, where the large bracket indicate hole states. The onset can be calculated to be about 706.7 eV, and the spectral shape was found to be very sensitive to the excitation energy. The peak intensities of these lines were carefully determined by a least-squares fitting.

In Fig. 7, the normalized intensities are plotted as a function of the incident photon energy together with the F-K XANES spectrum for comparison. Fig. 7 shows that the energy dependence of the total SXE yield (blue circles), given by $K\alpha_{1,2} + K\alpha L^1 + K\alpha L^2$ where $K\alpha L^n$ denotes a configuration with a single K vacancy and nL vacancies, looks very similar to the XAS. Thus it is apparent that the red circles give the F-K XAS free from the contribution of multielectron transitions, while the curve of the $K\alpha L^1$ yields (blue triangles) represents the excitation function of [1s2p] double excitation. This curve shows the double excitation of 1s and 2p electrons into the F 3p states forming the unoccupied t_{1u} molecular orbital, namely the [1s2p]3p^2 state. If we plot the energy-shifted $K\alpha L^1$ satellite intensity's evolution with ΔE = 26.7 eV to the lower energy side, we find a close resemblance between the energy-shifted $K\alpha L^1$ curve and the F-K XAS (Fig. 8). This energy shift ΔE = 26.7 eV is in fairly good agreement with theoretical energy difference 23.6 eV between the [1s]3p single excitation and the [1s2p]3p^2 double excitation. This would imply that the excitation function for the [1s2p] double excitation, although it locates at higher energy side due to the existence of a 2p spectator hole, represents the replicative excitation

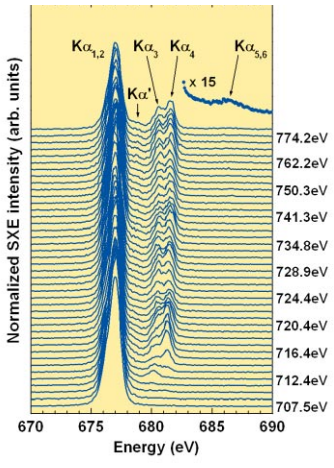

Figure 6
Spectral variation of the F Kα emission for NaF. Typical energies of the exciting photons are shown beside each spectrum.

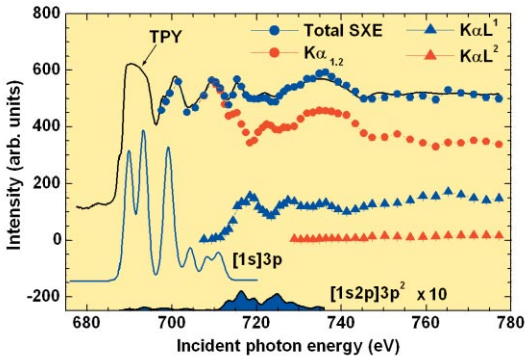

Figure 7.
The F-K absorption spectrum (upper solid line) of NaF measured by the TPY method. The normalized SXE yields are plotted as a function of the exciting photon energy. Theoretical fluorescence XANES spectra for the [1s]3p single excitation (lower solid line) and the [1s2p]3p^2 double excitation (solid line with shade) are also presented.

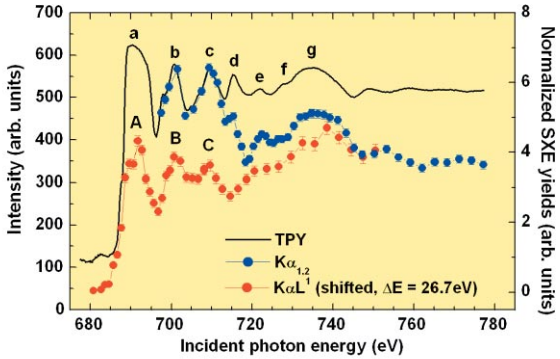

Figure 8.
The F-K absorption spectrum (thick solid line) of NaF compared with the evolution curves for the normalized SXE yields for the $K\alpha_{1,2}$ and $K\alpha L^1$ lines. The $K\alpha L^1$ satellite intensity's evolution is shifted along the energy axis by 26.7 eV to the lower energy side.

function reflecting that for single excitation. Such a phenomenon was predicted more than 30 years ago and the present study demonstrates evidence for the prediction.

The present results have elucidated that the structure observed above 710 eV in the F-K XANES spectrum of NaF does contain the contribution of multielectron transitions and it can be separated into each component by observing the satellite intensity's evolution with fine energy steps. This method should be applicable for all materials and give insight into understanding absorption spectrum in XANES region.

5-4-5 Fermi Surface of a Shape Memory Alloy of TiNi

TiNi is a technologically important shape-memory alloy. Upon cooling, it undergoes a martensitic transformation from a high-temperature B2 or β-phase to a monoclinic phase. Current interest has been on the precursor where anomalies in the elastic constants and phonon spectra are commonly observed in martensitic alloys. The origin of the phonon softening, indicated by inelastic neutron scattering, has long been speculated to be due to Fermi surface nesting. No direct experimental information about the geometry of the Fermi surface of the β-phase has yet been obtained.Recently, it has become possible to map out the three dimensional (3D) Fermi surface by reconstructing 3D electron momentum density from Compton scattering data [12].

Here, we present the occupation-number density in k-space (the first Brillouin zone) of $Ti_{48.5}Ni_{51.5}$ obtained from Compton scattering data, and examine the geometry and nesting feature of the Fermi surface [13]. An alloy ingot of $Ni_{51}Ti_{49}$ was prepared by repeated arcmelting in an argon atmosphere. A single crystal was grown from the ingot by a floating zone melting method. The martensitic transformation temperature M_s (A_f) was 170 K (210 K). The Compton profiles were measured at AR-NE1A1. The direct Fourier transform method [13] was applied to reconstruct the 3D electron momentum density $\rho(p)$. After obtaining $\rho(p)$, we employed the LCW-folding procedure to obtain the 3D occupation-number density in k-space.

Figures 9(a)-(c) show the contour maps of the occupation-number densities on the Γ-X-M, Γ-X-R-M and X-M-R planes, respectively, in the repeated zone scheme. The planes and symmetry points of the first Brillouin zone are shown in Fig. 9(d). The occupation-number density is the lowest at Γ and the highest at R and X, indicating the presence of a hole surface centered at Γ and electron surfaces at R and X. We can easily recognize the geometrical shape of the Fermi surface. Concerning the nesting features of the Fermi surface, by geometrical consideration of the contour pattern, we see some parallel or near parallel flat surfaces which suggest possible nesting. For intraband nesting of the parallel flat parts of the electron surface at R there are two nesting vectors, a in parallel with the R-M-R axis and *b* in parallel with the R-X-R axis (the arrows in

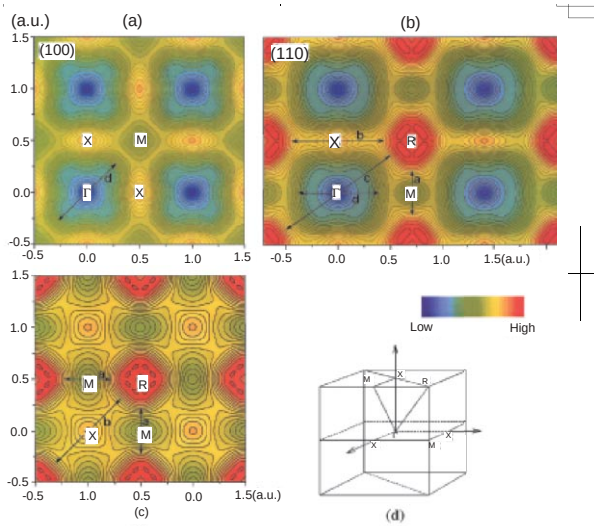

Figure 9.
Contour maps of the occupation-number densities on the Γ-X-M (a), Γ-X-R-M (b) and X-M-R (c) planes in the repeated zone scheme. The first Brillouin zone with high symmetry points is depicted in (d). The arrows indicate possible nesting vectors [13].

Fig. 9(c)), and a vector *c* in parallel with the R-Γ-R axis in Fig. 9(b). For another intraband nesting of the near parallel flat parts of the hole surface centered at Γ, there is a vector *d* in parallel with the Γ-M axis (Fig. 9(a)). Let us focus on the nesting vector *b* in the [110] direction, whose length is approximately 2/3[110]2π/a. By recalling the expression of the generalized susceptibility, it can be reduced to 1/3(110)2π/a by subtracting the [110] reciprocal lattice vector. Thus, we have succeeded, for the first time, in showing that the phonon softening originates from this nesting vector *b*.

5-4-6 Magnetic Circular Dichroism of Resonant X-ray Emission Spectroscopy in Sm-Co Amorphous Alloy

Electric quadrupolar (E2) transitions at the rare-earth (R) $L_{3,2}$-edges have attracted wide interest as an important subject for solid-state spectroscopy and for X-ray studies of magnetism, since the 4f final state of the $2p \rightarrow 4f$ quadrupolar transition is the dominant magnetic carrier of R elements. It has been widely believed that the E2 contribution has an absorption signal at the pre-edge regions of the $L_{2,3}$-edges, since the $4f$ level is pulled down below the dipolar (E1) absorption edge due to the strong Coulomb interaction between the $2p$ core hole and the $4f$ electrons. Although the E2 contributions are not normally visible in X-ray absorption spectroscopy (XAS) spectra due to their being superimposed on the E1 transition, they are significantly enhanced in magnetic circular dichroism (MCD) spectra (Fig. 10). However, confirmation of this has been a controversial subject for a long time due to the difficulty in collecting satisfactory evidence within the framework of first order optical processes such as MCD of XAS (MCDXAS).

The E2 transition has been studied by resonant X-ray emission spectroscopy (RXES). It is a great advantage of RXES that the E2 contribution can be separated from the E1 transition. RXES experiments at the Sm $L_{2,3}$-edges in $Sm_{21}Co_{79}$ were performed at BL-28B

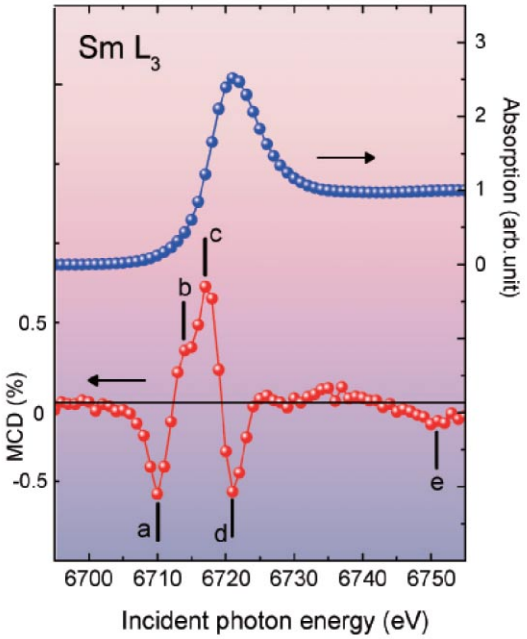

Figure 10
XAS (blue circles) and MCD (red circle) at the Sm L_3-edge in $Sm_{21}Co_{79}$ amorphous thin film at room temperature. Peaks *a* and *b* are attributed to orginate from the E2 contribution at the pre-edge region. Energies *c*, *d* and *e* correpond to on- and off-resonant energy regions at the L_3-edge. The MCDRXES were recorded at the energies labeled by a~e.

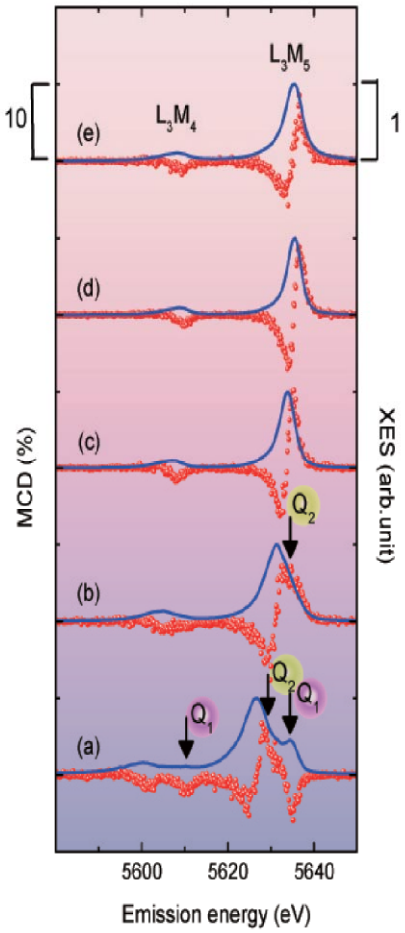

Figure 11
RXES (blue lines) and MCD spectra (red circles) for the Sm $L_3M_{4,5}$ edges. The labels a-e correspond to those in Fig. 10. RXES peaks labels Q_1 and Q_2 are due to the E2 transitions from *2p* to *4f*, where Q_1 and Q_2 are attributed be RXES which originate from the E2 excitation to the majority and minority of the Sm *4f* spin state, respectively

using an X-ray emission spectrometer. Fig. 11 shows MCD spectra of RXES (MCDRXES) recorded for the $L_3M_{4,5}$ edges, which correspond to the optical processes of the $3d \rightarrow 2p$ decay after the $2p \rightarrow 5d$ dipolar (E1) excitation and the $2p \rightarrow 4f$ quadrupolar (E2) excitation. In the MCDRXES spectrum at point (a) in Fig. 11, the E2 MCD features associated with Q_1 and Q_2 are observed with the negative and positive signs, respectively. The signs of peaks Q_1 and Q_2 in Fig. 11 are consistent with those of *a* and *b* in the MCDXAS in Fig. 10. For the MCDRXES spectrum of Q_1, the E2 contribution is the dominant origin of the corresponding MCDXAS, because the E1 part has a dispersive shape, the integration of which is almost zero. The observation of the negative peak and the positive shoulder of MCDRXES for the Q_1 and Q_2 signals represents direct identification of the E2 MCD at the pre-edge region and is exactly what we have expected to obtain.

To interpret the experimental results, theoretical calculations based on the formula of the coherent second order optical process have been carried out. The calculated MCDRXES spectra reproduce all the experimental results very successfully. The series of the present study has given the important knowledge of how we use the E2 transition for the study of the *4f* magnetism and how we interpret the result [14,15].

5-4-7 Oscillations of Surface Magnetization in Fe/Ni/Cu(100) Films Observed with the Depth-resolved X-ray Magnetic Circular Dichroism Technique

Ultrathin Fe films on Cu(100) have attracted much interest due to their characteristic magnetic depth profiles. We have developed a new technique, depth-resolved XMCD, in which the probing depth of the electron-yield XMCD is controlled by the electron detection angle [16]. If an Fe film is grown on a ferromagnetic substrate, the interface (bottom) layer interacts with the substrate, and one can expect some magnetic coupling between the surface and the interface via the inner layers. We have studied the magnetic structure of Fe films grown on a Ni/Cu(100) film with the depth-resolved XMCD technique [17,18].

Fe and Ni were deposited on a clean and ordered Cu(100) single crystal at room temperature. The sample was magnetized by a current pulse through a coil. The remanent magnetization was then investigated. A series of XMCD spectra with different probing depths were simultaneously recorded (Fig. 12) in the partial electron-yield mode. All the spectra were recorded at grazing X-ray incidence, since the present films exhibited in-plane magnetization in the remanent state.

Series of XMCD spectra from Fe(4-9 ML)/Ni(6 ML)/Cu(100) films are given in Fig.13(a) as a function of probing depth, λ_e. The spectra from the 4-ML Fe film are identical, irrespective of λ_e, indicating a uniform ferromagnetic structure. In contrast, the XMCD intensity from the 4.5-ML film drastically decreases with increasing λ_e. Moreover, the XMCD signal is opposite in sign to that

from the 4-ML film. These results show that the surface of the 4.5-ML film has a magnetization opposite to the applied field, and that its magnitude is larger than that of the inner layers. As the Fe thickness (t_{Fe}) increases, the XMCD signal almost vanishes at 6 ML, and reappears with opposite sign at 9 ML. The Ni film exhibited a positive magnetization independent of t_{Fe}.

The data were analyzed assuming that the Fe film consists of three regions; two surface layers, a single interface (bottom) layer, and the remaining inner layers [18]. The estimated surface and interface magnetizations are depicted in Fig. 13(b) as a function of t_{Fe}. The surface magnetization shows oscillatory behavior, while the interface one stays almost unchanged. The inner layers were almost nonmagnetic (<0.2μ_B). Note that the observed oscillation in the surface magnetization can be also interpreted as a rotation of the magnetic moment.

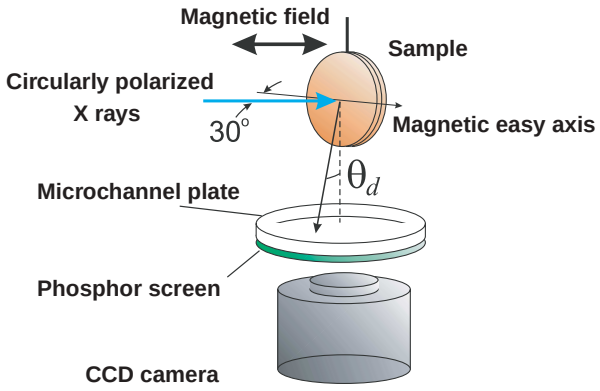

Figure 12.
Schematic layout of the depth-resolved XMCD measurement. A set of electron-yield XMCD spectra are recorded at different direction angles θ_d, which correspond to different probing depths.

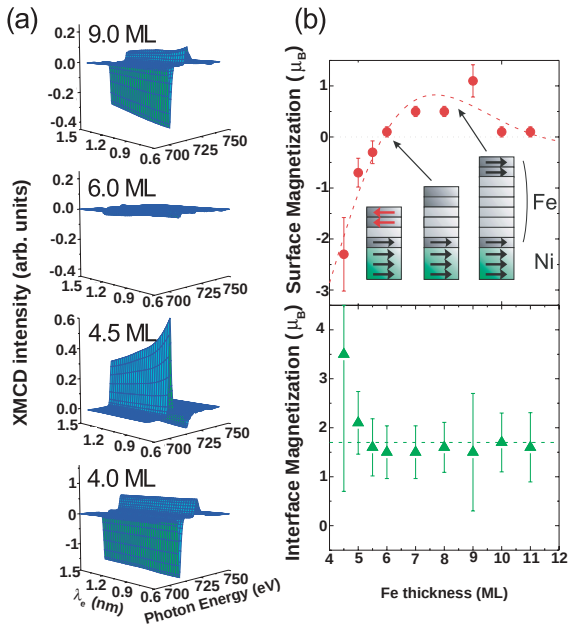

Figure 13
(a) Fe *L*-edge XMCD from Fe(4-9 ML)/Ni(6 ML)/Cu(100) films with different probing depths, λ_e., recorded at 200K. (b) Estimated surface and interface magnetization, with the deduced magnetic structure model.

If the surface magnetic moment rotates as a function of t_{Fe}, there should be two equivalent domains in which the moment rotates in clockwise and counterclockwise directions. The resultant magnetization should oscillate due to the averaging over the two domains. An oscillatory or rotational magnetic interaction is thus suggested between the surface and interface via the nonmagnetic inner layers.

5-4-8 Evidence for Room-Temperature Ferromagnetism Induced by Doped Co Ions in $Ti_{1-x}Co_xO_{2-\delta}$: An X-ray Magnetic Circular Dichroism Study

Dilute magnetic semiconductors (DMS) have attracted much scientific and technological interest as promising materials for spintronic devices. Since the discovery of room-temperature ferromagnetism in Co-doped TiO_2 [19,20], oxide magnetic semiconductors have been intensively studied. The origin of ferromagnetism remains controversial. Namely, it is still an open question whether the ferromagnetism originates from the intrinsic character or from segregated nano-scale magnetic impurities [21].

We have studied the origin of the reported ferromagnetism in Co-doped rutile-type TiO_2 [20] by making high-precision X-ray magnetic circular dichroism (XMCD) measurements at the Co $L_{3,2}$ edges on carefully prepared as-deposited samples using the PLD method. Ferromagnetism was confirmed at room temperature by the anomalous Hall effect and by magnetization measurements with a SQUID magnetometer [22]

Figure 14 shows the Co L_3-edge X-ray absorption (XAS) and XMCD spectra of the rutile-type $Ti_{0.97}Co_{0.03}O_{2-\delta}$ film. The spectra were recorded at room temperature with the total electron-yield method using circularly polarized soft X-rays. The XMCD spectrum of metallic Co is also shown in for comparison. The XAS shows multiplet features, denoted by arrows A to E. Multiplet features were also observed in the XMCD, corresponding to those in the XAS. What is the most remarkable in the XMCD is a clear negative peak corresponding to peak D in the XAS. No corresponding feature was seen in the XMCD of metallic Co. The dominant negative peak in the XMCD exhibits a line shape more flattened than that in the XMCD of metallic Co, indicating overlapping, unresolved multiplet features corresponding to features B and C in the XAS. The XMCD spectrum at the Co L_2 edge shows doublet features corresponding to a peak and a shoulder in the XAS. The present observation of multiplet features in the XMCD shows that the ferromagnetism originates from Co ions with localized d electrons, in sharp contrast to the result of a previous XMCD study [21].

Figure 15 shows a comparison of the experimental XMCD with the results of full atomic multiplet calculations. The calculations have been made for a low-spin and a high-spin Co^{2+} ion in the O_h crystal field, and a high spin Co^{2+} ion in the D_{2h} crystal field. The possibility of the Co^{2+} low-spin state in O_h symmetry is immediately

ruled out. The experimental XMCD spectrum shows qualitatively the best agreement with the calculated spectrum for the Co^{2+} high-spin configuration in D_{2h} symmetry. These results verify the intrinsic ferromagnetism induced by the high-spin Co^{2+} ions substituting the Ti^{4+} ions in $Ti_{0.97}Co_{0.03}O_{2-\delta}$.

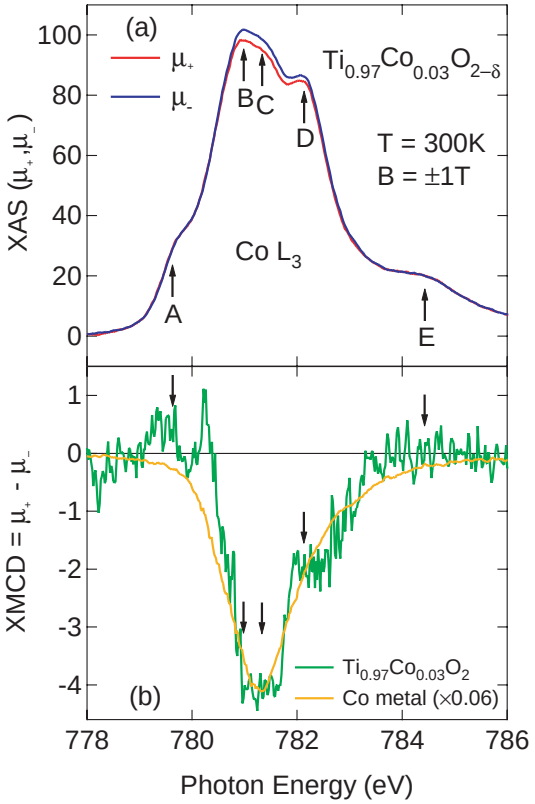

Figure 14
(a) Photon-helicity dependent Co L_3-edge X-ray absorption spectra (XAS) of rutile-type $Ti_{0.97}Co_{0.03}O_{2-\delta}$. (b) Co L_3-edge XMCD of rutile-type $Ti_{0.97}Co_{0.03}O_{2-\delta}$ (green curve). The XMCD spectrum of metallic Co is shown with a 0.06 scaling (orange) for comparison.

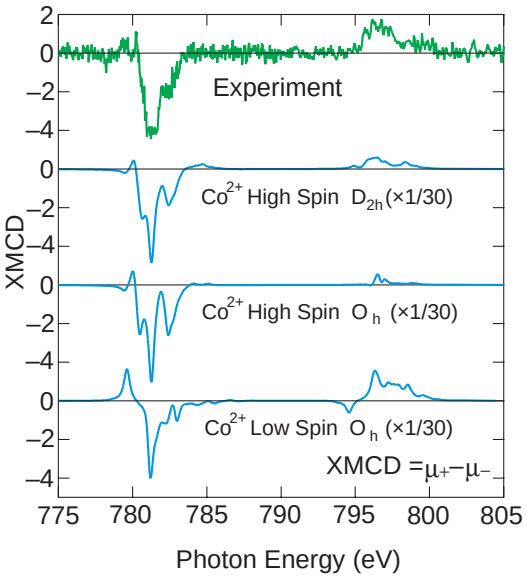

Figure 15
Comparison of the experimental XMCD (green curve) with atomic multiplet calculations (light blue curves). Calculations were made for the low-spin Co^{2+} ion and the high-spin Co^{2+} ion in the crystal field with O_h symmetry, and the high-spin Co^{2+} ion in the crystal field with D_{2h} symmetry. The calculated XMCD spectra have been scaled by a factor of 1/30 for comparison with the experimental XMCD spectrum.

5-4-9 Fabrication and Electronic Structures of Zinc-Blende Type Ferromagnet Grown by Molecular-Beam Epitaxy

Recently “spintronics”, that positively uses the electron spin in electronics, has attracted much attention and a search for new spintronic materials such as a half-metallic ferromagnet and a magnetic semiconductor becomes very active. We propose a new scheme for the search of spintronic materials, which is a combination of a materials design, a materials fabrication by molecular-beam epitaxy (MBE), and an in situ electronic structure characterization using photoemission.

We have succeeded in the growth of zinc-blende (zb) type ferromagnets MnAs and CrAs that have been

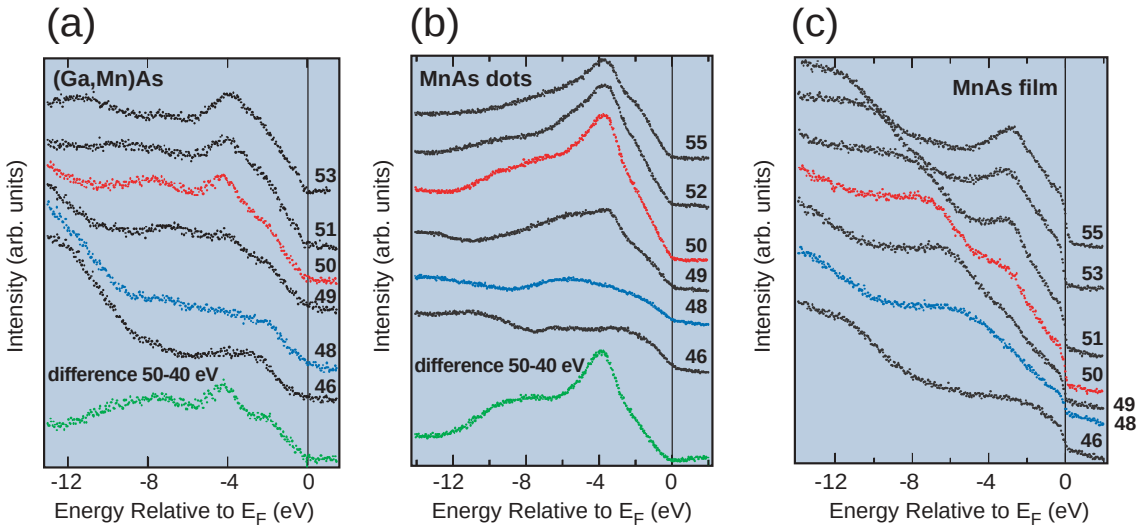

Figure 16
In situ photoemission spectra of (Ga,Mn)As, zinc-blende MnAs dots, and MiAs-type MnAs film.

predicted to be a half-metallic characteristics based on the first principles band calculation. MnAs dots and CrAs epitaxial films were grown by MBE and their electronic properties were measured by in situ synchrotron radiation photoemission spectroscopy (SRPES), respectively. Zb-type CrAs epitaxial films grown on GaAs (001) by MBE show a ferromagnetic property at room temperature with the magnetic moment of about 3 μB, suggesting the possibility of the half-metallic characteristics. The electronic structure of zb-CrAs obtained by SRPES agrees well with the first principles band calculation. Furthermore, sulfur termination of GaAs surfaces enabled the formation of zb-type MnAs dots. SRPES analysis shown in Fig. 16 reveals that the zb-MnAs dots show a distinctive valence band electronic structure with Mn 3d-related peak at about 4 eV of binding energy which is quite similar to that of (Ga,Mn)As, but different from the NiAs-type MnAs thin film.

5-4-10 High-Throughput Characterization of the Surface Electronic Structure of Strongly-Correlated Transition Metal Oxide Thin Films Using in-situ Photoemission Spectroscopy

Transition-metal oxide thin-films and superlattices attract much attention. Extensive studies of oxides films have demonstrated that the magnetic and electronic properties of the oxides can be controlled through interface utilizing spin exchange, charge transfer, and epitaxial strain. In order to investigate the surface and interface electronic structures of transition metal oxide thin films, we have constructed a system, which combines a high-resolution photoemission spectroscopy system with a combinatorial laser molecular-beam epitaxy (laser MBE) thin film growth system at BL-1C (Fig. 17). The distinctive feature of this system is the direct connection

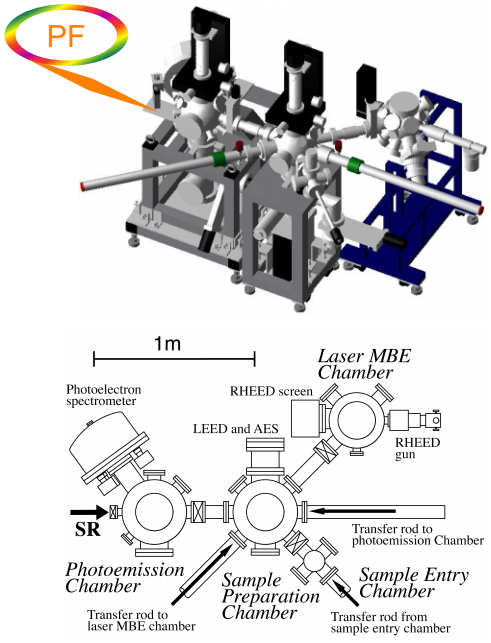

Figure 17
A schematic bird's eye view (top) and a layout diagram (bottom) of the "*in situ* HR-PES-laser MBE system"

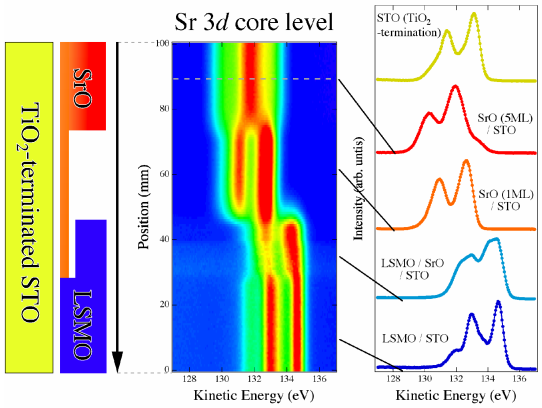

Figure 18
Cross-section schematics for the combinatorial library (left), Sr 3d core level imaging for the library (middle), and high-resolution Sr 3d core level spectra (right).

from the spectrometer to the combinatorial laser MBE chamber. The combinatorial laser MBE system can be used for fabricating combinatorial thin film libraries. We have characterized the electronic structure of a terminating-layer-controlled $La_{0.6}Sr_{0.4}MnO_3$ (LSMO) thin-film library fabricated on TiO_2-terminated $SrTiO_3$(001) (STO) substrates. By plotting the Sr 3d core level intensity as a function of both the kinetic energy and the beam position as shown in Fig. 18, we could find significant differences in the surface electronic structures of the library. Detailed analysis of the Sr 3d core-level reveals that the difference in the chemical bonding states of the Sr atoms in the surface regions stems from the difference in terminating layer of each film. These results show that the terminating layer of the LSMO films can be changed from an MnO_2 to an La/SrO layer by inserting one atomic layer of SrO between the LSMO film and a TiO_2-terminated STO substrate.

5-4-11 Half-Metallic Density of States in Sr_2FeMoO_6 Observed by Photoemission Spectroscopy

Tunneling magnetoresistance (TMR) phenomena have been getting more attention. To realize TMR, the electronic structure should ideally have a half-metallic density of states (DOS) with a high Curie temperature (Tc). Recently, Kobayashi et al. have reported that a double perovskite (DP) Sr_2FeMoO_6 showed a large TMR and also predicted a half-metallic DOS.

To understand the origin of TMR in Sr_2FeMoO_6, we have investigated the electronic structure using photoemission spectroscopy. Single crystals of Sr_2FeMoO_6 were grown by the floating-zone method, and the experiments were performed at BL-11D. Clean surfaces were obtained by fracturing samples in situ at 20 K.

In Fig. 19, the double peak structures *A* and *B* correspond to the Fe $e_{g\uparrow}$ and the Fe+Mo $t_{2g\downarrow}$ bands predicted by band theory. The behaviors of the spectral weights of *A* and *B* are quite different to each other. One can see that the spectral weight of *A* has a minimum at ~80 eV while such a clear minimum is not observed in *B*. Hence, the minimum of *A* can be interpreted as

the Cooper minimum of the Mo 4d states. This clearly demonstrates that *A* has a contribution from the Mo 4d states whereas *B* has only an undetectably small contribution. This is in perfect agreement with the prediction of band theories. It is, therefore, experimentally confirmed that only the down-spin band crosses E_F, and is half-metallic. The double-peak electronic structure is characteristic of Sr_2FeMoO_6 and is a key to understanding the half-metallic DOS of this compound. It is concluded that the unique properties of Sr_2FeMoO_6 can be explained by the strong Hund's rule coupling of the $3d^5$ configuration.

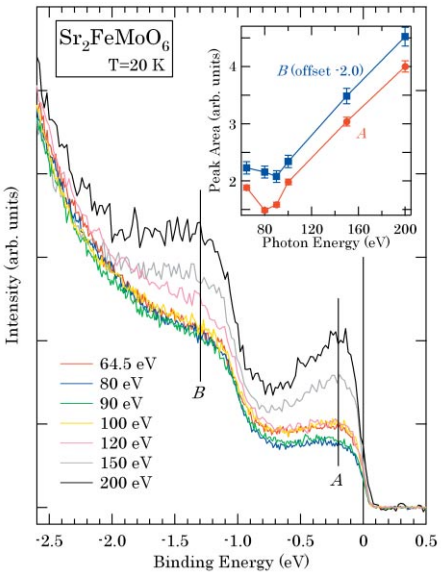

Figure 19
Photoemission spectra of Sr_2FeMoO_6 near the E_F region at T=20 K taken with several photon energies. Inset: Integrated intensitaies of peak *A* (at-0.20 ev) and *B* (at-1.30 eV) in 0.1 eV windows plotted as afunction of photon energy. Note that the curve for *B* has been offset by -2.0 to enable comparison with the curve for *A* on the same y scale.

5-4-12 Direct Observation of One-dimensional Electronic States in Single-wall Carbon Nanotubes

In one-dimensional (1D) metals, the Fermi-liquid states become unstable and electrons behave as a Tomonaga-Luttinger-liquid (TLL). Metallic single-wall carbon nanotubes (SWNTs) are considered to be ideal 1D systems with TLL states.

The electronic states of SWNT along the circumference are quantized so that peak structures due to 1D van Hove singularities (1D VHS) appear in the density of states (DOS). Photoemission experiments were performed at BL-11D of KEK-PF and BL-1 of HiSOR. SWNT samples with mean diameter of 1.37 nm were prepared by the laser vaporization method. The valence band spectrum of the SWNT is similar as a whole to that of graphite. The difference in spectral features appeared near the Fermi level (E_F) as shown in Fig. 20. For the SWNT sample, three peak structures, which correspond to the 1D VHS structures of semiconducting and metallic SWNTs, can be clearly seen.

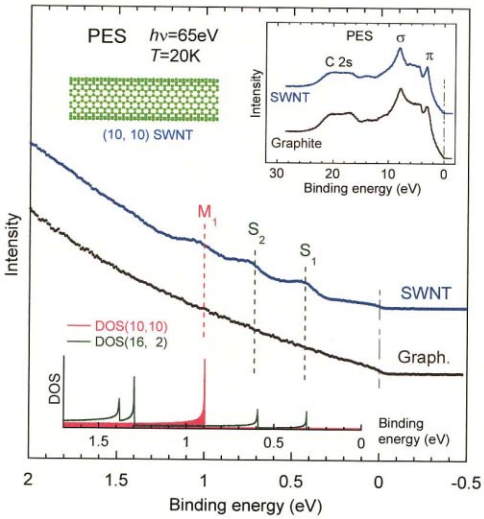

Figure 20 Photoemission spectra (PES) of SWNT sample and graphite. The densities of states (DOS) to SWNTs with chiral indices (10, 10) and (16, 2) are also shown. The spectrum of the SENT sample was shifted toward a higher binding energy by 0.1 eV because of doping of the SWN

Figure 21
Photoemission spectra (PES) of SWNT sample near

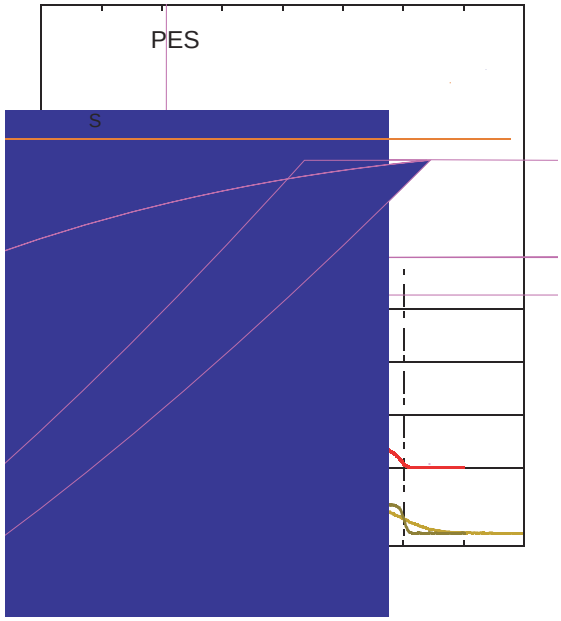

A solid line indicates ω

broadened by the energy resolution (Δ

to the intensity of the S1 peak. In high-resolution photoemission

Fig. 21, the photoemission intensity de

near

, which is different from that of Au. The origin of

the peculiar spectral feature is considered as the sup-

pression in DOS near due to a TLL state. The expo-

nent of the spectral function was estimated to be 0.46

± 0.10 which is almost the same as the exponent for

meV). The inset shows the temperatures dependence of the r

temperature 0.48±0.08. These power-law behaviors are consistent with both the theoretical calculation and the previous transport experiments. In conclusion, we have found direct evidence that a TLL state is realized in

5-4-13 Combinatorial in situ Photoemission Spectroscopy of Strongly Correlated Oxide Heterointerfaces

Superlattices based on transition-metal oxides have attracted much attention because of the possibility of tuning the magnetic and electronic properties of a thin film. To design devices, it is critically important to understand the electronic structure of oxide heterointerfaces. For the interface electronic structure analysis of these superlattices, we have employed an in situ photoemission spectroscopy system combined with a combinatorial laser molecular beam epitaxy (laser MBE) thin film growth system at BL-2C [23].

We have determined the compositional change in the electronic structures of $La_{0.6}Sr_{0.4}FeO_3$ (LSFO)/ $L_{0.6}Sr_{0.4}MnO_3$ (LSMO) super-lattices. For determining the interfacial electronic structure, we performed Mn 2p-3d resonant photoemission (RPES) measurements to extract the Mn 3d partial density of states (PDOS) of the LSMO layers in the vicinity of the interface with the LSFO overlayer.

In Fig. 22, the Mn 3d spectra consist of two prominent peaks, which are assigned to the Mn 3d $t_{2g}\uparrow$ and $e_g\uparrow$states. The spectra show an interesting change in spectral intensity near E_F, reflecting the modulated electronic structure at the interface. The reduction of the spectral intensity of the $e_g\uparrow$ states with increasing LSFO overlayer thickness therefore clearly indicates the occurrence of electron transfer from LSMO to LSFO layers in the interface region.

These results show that an intrinsic “dead layer” exists at the LSFO/LSMO interface due to the interfacial charge transfer between the 3d levels of the constituent transition metals.

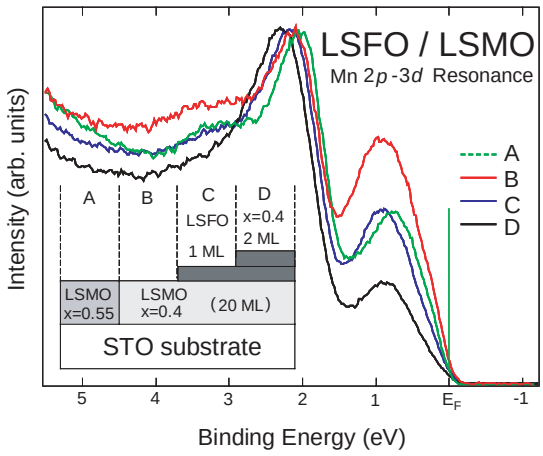

Figure 22
Mn 3d spectra of LSMO layers in the vicinity of an interface with LSFO. Mn 3d spectra of LSMO (x=0.4(B) and 0.55 (A)) films are also presented for comparison. The inset shows schematic side views of the measured libraries A-D.

5-4-14 Antiferromagnetic Domain Imaging of NiO(100) by PEEM, and the Non-magnetic Linear Dichroism Effect at the O K Edge

NiO is known as a typical antiferromagnetic (AFM) material. Below T_N, the crystal structure is slightly deformed along <111> axes. Crystallographic twinning leads to the so-called T(*win*)-domains. Each *T*-domain has an easy axis along [211]-derived directions and is split into S(*pin*)-domains. Photoelectron emission microscopy (PEEM) with synchrotron radiation, combined with magnetic linear dichroism (MLD) at the Ni L_2 edge has used for the study of the AFM domain structure of cleaved NiO(100) surfaces.

We have observed similar AFM domains of NiO(100) with MLD-PEEM near the O K edge at BL-2C, 11A and 13C. This result was unexpected, because the O atom should not have any magnetic moment. It is not clear whether the crystal distortion effect is essential to the non-magnetic LD or not. We have investigated the dependence on deposition of magnetic metal films on to the substrate.

Figure 23 shows the PEEM image in Fe(wedge)/ NiO system. In the lower coverage region, the domain seems similar, reflecting mainly the AFM domain of the NiO substrate. However, in the higher coverage region, the PEEM image observed at the Ni L_2-edge is strongly affected and has almost disappeared compared to the image obtained at the O *K edge*. If the twinned structure of the crystal is essential for the domain observed at the O *K edge*, the image should not be affected by the metal deposition. In contrast, the observed image at the Ni L_2-edge may easily be affected by metal deposition. Therefore, it is suggested that the AFM domain structure, observed at the O *K edge*, reflects the T-domain and that the crystal distortion is essential. Probably due to the exchange coupling at the interface, the S-domain is strongly affected whereas the T-domain is only weakly affected.

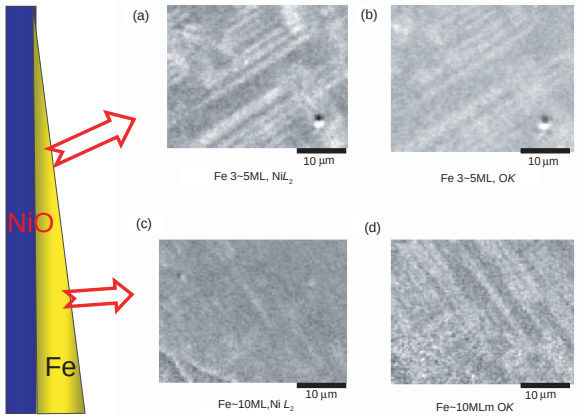

Figure 23
AFM domain images of wedge-shaped Fe covered surfaces of NiO(100). (a) image at the Fe 3-5 ML regio nobserved at the Ni L_2 edge. The ratio of two images recorded at 870.2 eV and 871.5 eV is taken in order to obatin a clear AFM domain contrast. (b) Same as in (a) but at the O *K* edge (528.3 eV and 537.0 eV).(c) Same as in (a) but at the Fe -10ML region. (d) Same as in (c), but at the O *K* edge.

References

[1] A. Kotani and S. Shin, *Rev. Mod. Phys.,* **73** (2001) 203.
[2] Y. Harada et al., *J. Syncrotron Rad.,* **5** (1998) 1013.
[3] Y. Harada et al., *Phys. Rev. B,* **61** (2000) 12854.
[4] M. Matsubara et al., J. *Phys. Soc. Jpn.,* **69** (2000) 1558.
[5] A.Y. Liu and M.L. Cohen, *Science,* **245** (1989) 841.
[6] I. Shimoyama et al., *Phys. Rev. B,* **62** (2000) R6053; *J. Elec. Spectrosc. Relat. Phenom.,* **114-116** (2001) 841.
[7] J. Nagamatsu et al., *Nature,* **410** (2001) 63.
[8] T. Oguchi, *J. Phys. Soc. Jpn.,* **71** (2002) 1495.
[9] J. Nakamura et al., *J. Phys. Soc. Jpn.,* **71** (2002) 408.
[10] M. Oura et al., *J. Phys. B,* **35** (2002) 3847.
[11] M. Oura et al., Phys. *Rev. Lett.,* **90** (2003) 173002.
[12] Y. Tanaka et al., *Phys. Rev. B*, **63** (2001) 045120.
[13] N. Shiotani et al., *J. Phys. Soc. Jpn.*, **73** (2004) 1627.
[14] T. Nakamura et al.,*Phys. Rev. B*, **67** (2003) 094439
[15] K. Fukui and A. Kotani, *J. Phys. Soc. Jpn.*, **73** (2004) 1059.
[16] K. Amemiya et al., *Appl. Phys. Lett.*, **84** (2004) 936.
[17] K. Amemiya et al., *Phys. Rev. B*, **70** (2004) 195405.
[18] K. Amemiya et al., *J. Electron Spectrosc. Relat. Phenom.*, **144** (2005) 689.
[19] Y. Matsumoto et al., *Science*, **291** (2001) 854
[20] Y. Matsumoto et al., *Jpn. J. Appl. Phys.*, **40** (2001) L1204.
[21] J. -Y. Kim et al., *Phys. Rev. Lett.*, **90** (2003) 017401.
[22] H. Toyosaki et al, *Nature Materials*, **3** (2004) 221.
[23] K. Horiba, H. Ohguchi, H. Kumigashira, M. Oshima, K. Ono, N. Nakagawa, M. Kippmaa, M. Kawasaki and H. Koinuma, *Rev. Sci. Instrum.*, **74** (2003) 3405.